nature physics

Article

https://doi.org/10.1038/s41567-025-03023-3

Pressure induced superconductivity in hybrid Ruddlesden–Popper $La_5Ni_3O_{11}$ single crystals

Received: 4 February 2025

Accepted: 4 August 2025

Published online: 05 September 2025

Check for updates

Mengzhu Shi[1,2,9], Di Peng[3,4,9], Kaibao Fan[1,2], Zhenfang Xing[4], Shaohua Yang[5], Yuzhu Wang[6], Houpu Li[1,2], Rongqi Wu[1,2], Mei Du[1,2], Binghui Ge[5], Zhidan Zeng[4], Qiaoshi Zeng[3,4] ✉, Jianjun Ying[1,7], Tao Wu[1,2,7,8] ✉ & Xianhui Chen[1,2,7,8] ✉

The discovery of high-temperature superconductivity under high pressure in Ruddlesden–Popper phase nickelates has captured notable attention in the condensed matter physics community. Here we report superconductivity in a distinct hybrid nickelate, $La_5Ni_3O_{11}$, formed by alternating stacks of $La_3Ni_2O_7$ and La_2NiO_4 layers. This nickelate also exhibits a density-wave transition at approximately 170 K near ambient pressure. With increasing pressure, this density-wave transition shifts to higher temperatures and abruptly disappears around 12 GPa, followed by the emergence of superconductivity, indicating a first-order phase transition. But the optimal superconductivity with large superconducting volume fraction is observed at approximately 21 GPa with T_c^{zero} = 54 K. High-pressure X-ray diffraction experiments reveal a structural phase transition from an orthorhombic structure to a tetragonal structure at lower pressure. Notably, this structural change has minimal impact on the density-wave or superconducting phases, suggesting a limited role of lattice degrees of freedom in this material. These findings establish $La_5Ni_3O_{11}$ as a new superconducting member of the Ruddlesden–Popper nickelate family and offer valuable insights into the interplay between structure, electronic order and superconductivity in hybrid nickelates.

Since the discovery of superconductivity in cuprates, exploring high-temperature superconducting materials with similar crystal and electronic structures has become an important research direction[1–7]. A major breakthrough in this field was made in the infinite-layer nickelate $Nd_{0.8}Sr_{0.2}NiO_2$ thin films with a superconducting transition temperature (T_c) of 9–15 K in 2019[8]. Motivated by this groundbreaking finding, the Ruddlesden–Popper (RP) phase nickelates $R_{n+1}Ni_nO_{3n+1}$ (*R*, rare earth) with $n = 2$ and $n = 3$ are reported to exhibit superconductivity under pressure[9–13], which largely expands the family of nickelate superconductors. In these RP nickelates $R_{n+1}Ni_nO_{3n+1}$, the multilayer perovskite structure $(RNiO_3)_n$ is believed to be the fundamental building block for superconductivity. Clarifying the role of the multilayer perovskite structure $(RNiO_3)_n$ in the superconducting phase is important for building a theoretical model for the superconducting mechanism. At ambient pressure, the NiO_6 octahedron in the $(RNiO_3)_n$ structure is distorted and tilted, which leads to an orthorhombic structure. Moreover, in such an orthorhombic structure phase, a density-wave (DW) transition is widely observed at approximately 130–150 K in RP nickelates with $n = 2$ and $n = 3$, which involves both spin- and charge-density-wave orders[14–16]. With increasing pressure, the distortion and tilting of the NiO_6 octahedron are strongly suppressed, and a pressure-induced structural transition from an orthorhombic structure to a tetragonal structure

A full list of affiliations appears at the end of the paper

https://doi.org/10.1038/s41567-025-03023-3

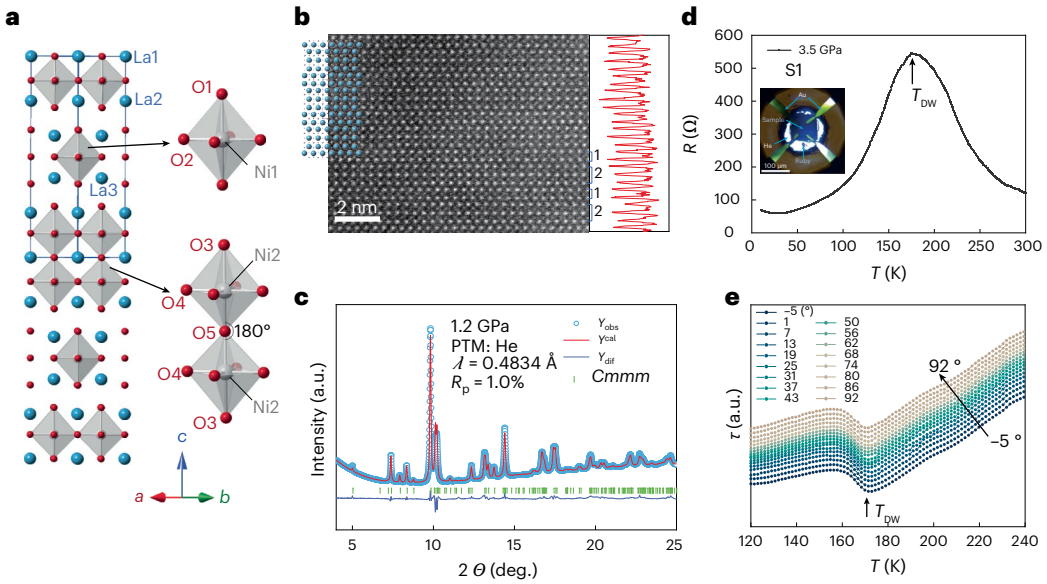

Fig. 1 | Structure and physical properties of $La_5Ni_3O_{11}$. a, Crystal structure model of $La_5Ni_3O_{11}$ (left panel) and the stacking units of the monolayer and bilayer NiO_6 octahedrons (right panel) solved from the single-crystal XRD data. The bond angle of Ni2–O–Ni2 in the bilayer subslab along the *c*-axis direction is 180°. **b**, Cross-sectional STEM image of $La_5Ni_3O_{11}$ along the [110] direction. There is clear monolayer (denoted as '1') and bilayer (denoted as '2') subslab stacking along the *c*-axis direction. The overlaid crystal structure model fits well with the STEM-HAADF image (left panel). The red curve in the right panel illustrates the integration of intensity across horizontal pixels for the image displayed in the left panel. The blue, grey and red balls for the crystal structure in the left panel represent the La, Ni and O atoms, respectively. **c**, Powder XRD pattern (blue circles) collected by grinding several microcrystals of $La_5Ni_3O_{11}$ at a moderate pressure of 1.2 GPa with a wavelength of 0.4834 Å. Adopting the Rietveld refinement method, the powder XRD pattern can be well fitted (red lines) via the structural model shown in **a**. The blue lines indicate the difference between the observed and calculated data. The short green vertical lines indicate the calculated diffraction peak positions. **d**, The temperature-dependent resistivity curve of $La_5Ni_3O_{11}$ at a small pressure (3.5 GPa) on the DAC when helium gas is used as the pressure-transmitting medium. The inset shows the sample connected with the gold electrodes inside the gasket hole. There is a large hump at approximately 170 K in the $R(T)$ curve, which resembles that of the previously reported electrical transport data collected on powder samples at ambient pressure. **e**, Temperature-dependent magnetic torque data ($\tau(T)$) for $La_5Ni_3O_{11}$ at various angles. There is a kink at approximately 170 K in the $\tau(T)$ curve, which is consistent with the anomaly in the $R(T)$ curve shown in **d**. These results indicate a possible DW transition in $La_5Ni_3O_{11}$ at approximately 170 K.

occurs at approximately 15 GPa (refs. 9,11,12). Previous high-pressure transport measurements suggest that the DW transition is also suppressed with increasing pressure, and the pressure-dependent phase diagram of superconductivity and DW order suggests a possible competing scenario with a second-order manner[9,17].

In addition to RP-phase nickelates, hybrid RP-phase nickelates have also been reported[18–20]. Hybrid RP-phase nickelates are formed by alternate stacking of different RP phases along the *c* axis. To date, two hybrid RP-phase nickelates have been reported: the 1313 phase, with a chemical formula of $La_3Ni_2O_7$, and the 1212 phase, with a chemical formula of $La_5Ni_3O_{11}$ (refs. 18–20). In the 1313 phase, the $(LaNiO_3)_3$ layer and La_2NiO_4 layer alternately stack along the *c* axis and are separated by the LaO layer. Previous high-pressure transport measurements suggest possible high-temperature superconductivity in the 1313 phase, with an onset transition temperature of approximately 80 K (ref. 20). Since there are no reports on superconductivity in the La_2NiO_4 phase, the superconducting pairing should come from the $(LaNiO_3)_3$ layer. This result further supports the use of the multilayer perovskite structure $(RNiO_3)_n$ as the fundamental building block for superconductivity. However, there is a hot debate on the superconducting phase for pressurized superconductors with the chemical formula $La_3Ni_2O_7$ and the onset transition temperature $T_c^{onset} = 80$ K because this chemical formula can share either the RP phase $R_{n+1}Ni_nO_{3n+1}$ with $n = 2$ or the hybrid RP 1313 phase, which is formed by alternate stacking of the $(LaNiO_3)_3$ layer and the La_2NiO_4 layer along the *c* axis. Furthermore, $T_c^{onset} = 80$ K in the hybrid RP 1313 phase seems to conflict with the reported superconductivity with a T_c^{onset} of less than 30 K in the pressurized RP trilayer nickelate $La_4Ni_3O_{10}$ (refs. 10–13); more experiments on the origin of superconductivity in the 1313 phase are needed. Because the multilayer perovskite structure $(RNiO_3)_n$ serves as the fundamental building block for superconductivity, high-temperature superconductivity should be expected in the 1212 phase under pressure. In the 1212 phase, as shown in Fig. 1a, the single-layer and bilayer blocks of NiO_6 octahedron alternately stack along the *c* axis, forming the so-called hybrid RP 1212 nickelate[18]. In this work, we perform a systematic study of the pressure-dependent evolution of the electronic state in a hybrid RP 1212 nickelate single crystal with a chemical formula of $La_5Ni_3O_{11}$. High-pressure transport measurements using helium gas as the pressure-transmitting medium revealed an unambiguous superconducting transition above ~12 GPa. The optimal superconducting transition temperature of a T_c^{onset} of ~64 K and a zero-resistivity temperature (T_c^{zero}) of ~54 K are achieved at approximately 21 GPa. The notable Meissner effect confirms bulk superconductivity under high pressures, with a superconducting volume fraction as high as 70%. In addition, the pressure-dependent evolution of the superconductivity, DW transition and structure are also mapped out.

Structure and density-wave transition at nearly ambient pressure

The hybrid RP 1212 nickelate single crystal was synthesized through a molten-salt method (see Methods for details). After the flux was dissolved in water, the product was filtered with 400-mesh (~38.5 μm) sieves. A single crystal with typical dimensions of 0.1 × 0.1 × 0.02 mm was carefully checked via a four-circle diffractometer. Figure 1a shows the crystal structure model of the as-grown hybrid RP 1212 nickelate single crystal (left panel) determined from single-crystal X-ray diffraction (SC-XRD) data, where single-layer and bilayer perovskite-like NiO_6 octahedrons alternately stack along the *c*-axis direction, as previously reported[18]. The space group is determined to be *Cmmm*, which is different from the previously reported *Immm*[18]. We note that the similar

https://doi.org/10.1038/s41567-025-03023-3

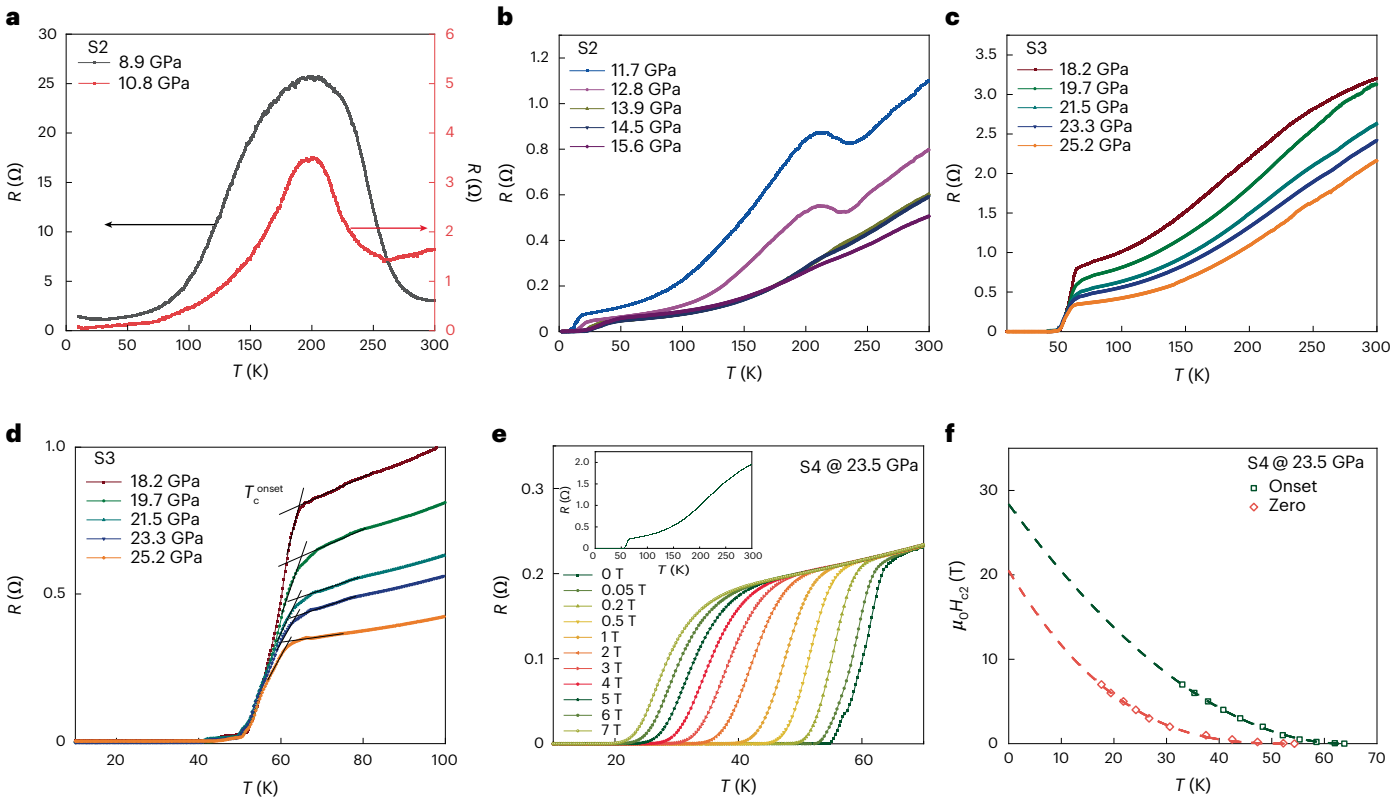

Fig. 2 | Electrical transport properties of $La_5Ni_3O_{11}$ single crystals under various pressures for three samples, S2, S3 and S4. a, $R(T)$ curves for $La_5Ni_3O_{11}$ (S2) in a relatively lower pressure range (8.9–10.8 GPa). **b**, $R(T)$ curves for $La_5Ni_3O_{11}$ (S2), where superconductivity begins to occur. **c**, $R(T)$ curves of $La_5Ni_3O_{11}$ (S3) with zero resistance at ~40 K at pressures above 18.2 GPa. **d**, Enlarged view of **c**, where the T_c^{onset} is defined graphically. **e**, $R(T)$ curves for $La_5Ni_3O_{11}$ (S4) under various magnetic fields along the *c*-axis direction. The onset T_c is quickly suppressed to a lower temperature with increasing magnetic field. The inset shows the $R(T)$ curve at 23.5 GPa without applying the magnetic field for the $La_5Ni_3O_{11}$ crystal (S4), which has similar electrical transport behaviour to that of sample S3 and shows a T_c^{onset} at ~64 K and a T_c^{zero} at ~54 K. **f**, The upper critical field extracted from **e**. There is an obvious positive curvature in the H_{c2}–T_c curve. The upper critical field at the zero-temperature limit is fitted via the two-band model at the clean limit with the equation $H_{c2}(T) = H_c(0) \times (1 - (T/T_c))^{1+\alpha}$, where $H_{c2}(0)$ and α are fitting parameters[21].

compound '1313'-phase nickelate, where single-layer and trilayer blocks of NiO_6 octahedrons stack alternately along the *c*-axis direction, also adopts a *Cmmm* space group[19]. The structure of the hybrid RP 1212 nickelate is also confirmed by atomically resolved scanning transmission electron microscopy (STEM) images, where the alternate stacking of single-layer and bilayer blocks of NiO_6 octahedrons is clearly observed in Fig. 1b. The overlaid crystal structure model fits well with the STEM high-angle annular dark-field (HAADF) image (Fig. 1b left panel). By grinding several pieces of hybrid RP 1212 nickelate single crystals, powder X-ray diffraction (XRD) patterns were collected at the Shanghai Synchrotron Radiation Facility at a wavelength of 0.4834 Å at moderate pressure (1.2 GPa) using helium gas as the pressure-transmitting medium. With the Rietveld refinement method, the powder XRD pattern can be well fitted with the structural model solved from the SC-XRD data. No other RP phase was observed in the powder XRD pattern. In the hybrid RP-phase nickelate $La_5Ni_3O_{11}$, the out-of-plane Ni–O–Ni angle between the NiO_6 octahedrons is symmetry-constrained to 180° (Fig. 1a and Extended Data Table 1), which is different from the value of 168° in $La_3Ni_2O_7$ with the *Amam* space group at ambient pressure. The out-of-plane Ni–O–Ni angle was previously thought to be critical for interlayer coupling between NiO planes, which favours superconductivity under high pressure. More detailed crystal data, structure refinements and bond angles are shown in the Extended Data Table 1 and Extended Data Fig. 1. To obtain good electric contact, the temperature-dependent resistivity curve ($R(T)$) for the as-grown microcrystal was measured on a diamond anvil cell (DAC) with a small pressure (~3.5 GPa) (see the inset of Fig. 1d). As shown in Fig. 1d, the resistance curve ($R(T)$) exhibits a large hump at approximately 170 K, which is consistent with a previous report on powder samples at ambient pressure[18]. The anomaly in the resistivity curve is possibly due to a DW transition, which is similar to the other RP phase nickelates and the hybrid RP '1313'-phase nickelate[14,15,19]. Magnetic torque measurements conducted on the hybrid RP 1212 nickelate microcrystal (Fig. 1e) confirmed a DW transition at ~170 K, which corresponds to the temperature at the maximum of the hump in the $R(T)$ curve. We note that no obvious non-stoichiometry is observed on the basis of the energy-dispersive X-ray spectroscopy (EDX) analysis (Extended Data Fig. 2) and the refinement of the SC-XRD data (Methods).

Pressure-induced superconductivity

The electrical transport properties of the hybrid RP 1212 nickelate under various pressures were collected on a DAC using helium gas as the pressure-transmitting medium[11]. Notably, the homogeneity of the pressure environment is very important for electrical transport measurements under pressure, especially for the hybrid RP 1212 nickelate. Owing to the large volume shrinkage of helium gas under high pressure, good electric contact is quite challenging in practice, and realistic electric contacts usually work well only within a limited pressure range. Here we successfully measured the electrical transport in different pressure ranges on four pieces of $La_5Ni_3O_{11}$ single crystals, S1, S2, S3 and S4, which were selected from the same batch. The electric contacts for samples S1 and S2 are good only for electrical measurements at relatively low pressures (below ~15 GPa), and the electric contacts for samples S3 and S4 are good only for electrical measurements at relatively high pressures (above ~15 GPa). For sample S2, the resistance at room temperature gradually decreases at a relatively low pressure

https://doi.org/10.1038/s41567-025-03023-3

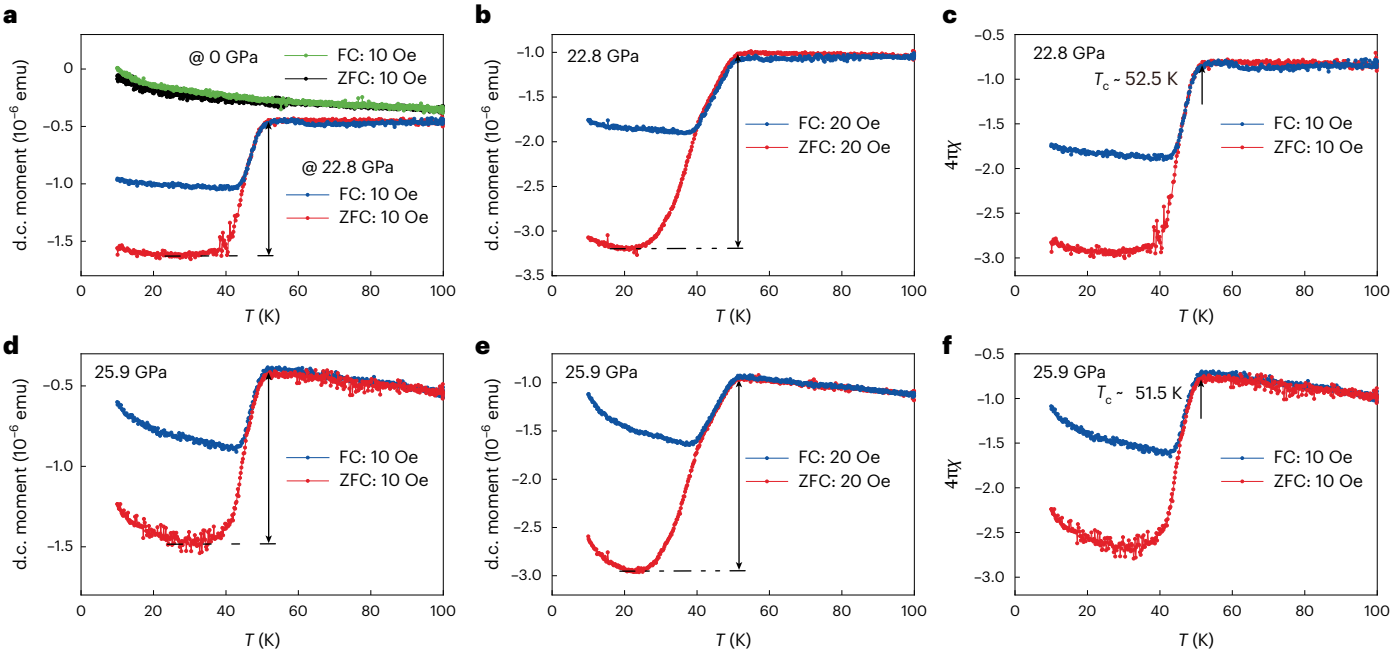

Fig. 3 | Temperature-dependent magnetic susceptibility of $La_5Ni_3O_{11}$ under high pressure. a,**b**, Temperature-dependent magnetic susceptibility at 22.8 GPa with magnetic fields of 10 Oe (**a**) and 20 Oe (**b**), respectively. **c**, The superconducting volume fraction curve calculated from **a** without the correction of the demagnetization factor. **d**,**e**, Temperature-dependent magnetic susceptibility at 25.9 GPa with magnetic fields of 10 Oe (**d**) and 20 Oe (**e**), respectively. **f**, The superconducting volume fraction curve calculated from **d** without the correction of the demagnetization factor. The black and green curves in **a** are measured at ambient pressure at a magnetic field of 10 Oe, which is regarded as the background signal. After the pressure is applied, there is a sharp transition at approximately 52.5 K at 22.8 GPa and 51.5 K at 25.9 GPa, which indicates the Meissner effect. The superconducting volume is estimated on the basis of the largest magnetic susceptibility difference between the normal state and the superconducting state (see the black arrows). The contribution from the Meissner effect is estimated to be ~1.16×10^{-6} emu and ~2.18×10^{-6} emu for zero-field cooling (ZFC) curves with magnetic fields of 10 Oe and 20 Oe at 22.8 GPa, respectively. The size of the sample is estimated to be a flat cylinder with a diameter of 210 ± 5 μm and a thickness of 20 ± 1 μm. The demagnetization factor is estimated to be $N^{-1} = 1 + 1.6 \times (C/A)$, where A is the diameter and C is the thickness of the sample[29,30]. The N is calculated as 0.8678. The superconducting volume fraction (SF) is corrected via the formula $SF = \chi/(1 - N \times \chi)$, where χ is the magnetic susceptibility without considering the demagnetizing factor. After the demagnetization factor is corrected, the superconducting volume fraction for ZFC (FC) curves at 22.8 GPa are estimated to be 74.5 ± 2.0% and 72.8 ± 1.8% (53.7 ± 2.8% and 42.9 ± 1.8%) with magnetic fields of 10 Oe and 20 Oe, respectively. The superconducting volume fraction for ZFC (FC) curves at 25.9 GPa are estimated to be 69.7 ± 2.1% and 70.0 ± 2.0% (42.5 ± 2.2% and 32.9 ± 2.0%) with magnetic fields of 10 Oe and 20 Oe, respectively. A more detailed error bar analysis is presented in Methods.

(8.9–10.8 GPa; Fig. 2a), and the overall temperature-dependent behaviour is similar to that of sample S1 at 3.5–7.6 GPa (Fig. 1d and Extended Data Fig. 3). When the applied pressure further increases above 11.7 GPa, although the DW transition temperature remains almost unchanged, the signature of the DW transition in transport is strongly suppressed and completely fades above ~13 GPa (Fig. 2b). This result suggests a pressure-induced first-order phase transition for the DW order. At ~11.7 GPa, a sharp drop in the $R(T)$ curve indicates the emergence of superconductivity, with a T_c^{onset} of 17.9 K (Fig. 2b). Above 11.7 GPa, the value of T_c^{onset} continuously increases and reaches the optimal superconductivity, with the highest T_c^{onset} value of ~64 K occurring at ~21.5 GPa (Fig. 2c,d, sample S3). As shown in Fig. 2d, there is a step-like transition at approximately 50 K due to possible inhomogeneity of the pressure environment, which leads to a zero-resistance temperature of only 42 K in sample S3 (Extended Data Fig. 4a). By improving the homogeneity of the pressure environment, we finally obtain a T_c^{onset} of ~64 K and a T_c^{zero} of ~54 K for sample S4 (Fig. 2e), which are among the highest reported zero-resistance temperatures and the sharpest superconducting transitions for nickelate superconductors, to our knowledge. As shown in Fig. 2e and Extended Data Fig. 4, we studied the superconducting transition under different magnetic fields perpendicular to the *ab* planes. The T_c quickly decreases to a lower temperature as the magnetic field increases to 7 T, which is a typical characteristic of superconductivity. The upper critical field (H_{c2}) is extracted with different criteria. As shown in Fig. 2f, there is a positive curvature in the H_{c2}–T_c curve, which cannot be explained by a single-band Ginzburg–Landau model. Here we use a two-band model at the clean limit to fit the upper critical field, which works quite well and yields H_{c2} values of 20–28 T at the zero-temperature limit[21]. In $La_3Ni_2O_7$ with the *Amam* space group, the upper critical field along the out-of-plane direction is ~180 T at 18.9 GPa[9], which is much greater than that in our case. This low upper critical field in the hybrid RP 1212 nickelate is also confirmed in another single-crystal sample (Extended Data Fig. 4b). Above 20 GPa, the superconducting transition temperature starts to slightly decrease with increasing pressure, up to 25.2 GPa.

To confirm the bulk superconductivity by the Meissner effect, magnetic susceptibility measurements under high pressure are conducted by using helium gas as the pressure-transmitting medium on a magnetic property measurement system (see details in Methods). As shown in Fig. 3a, there is a sharp transition at 52.5 K in the magnetic susceptibility curve with zero-field cooling and field cooling at 22.8 GPa and an applied magnetic field of 10 Oe, compared with the background data at ambient pressure, which indicates a notable Meissner effect due to superconductivity. By considering the demagnetization factor, the superconducting volume fraction in zero-field cooling is calculated to be as high as 74.5% and 72.8% at 10 Oe (Fig. 3a) and 20 Oe (Fig. 3b) under 22.8 GPa, respectively. This clearly indicates the bulk nature of the superconductivity. More magnetic susceptibility measurements under a high pressure of 25.9 GPa during zero-field cooling and field cooling with the applied magnetic fields of 10 Oe and 20 Oe are shown in Fig. 3d,e, respectively. Figure 3d,e show a sharp transition at 51.5 K, where the superconducting volume fraction during zero-field cooling

https://doi.org/10.1038/s41567-025-03023-3

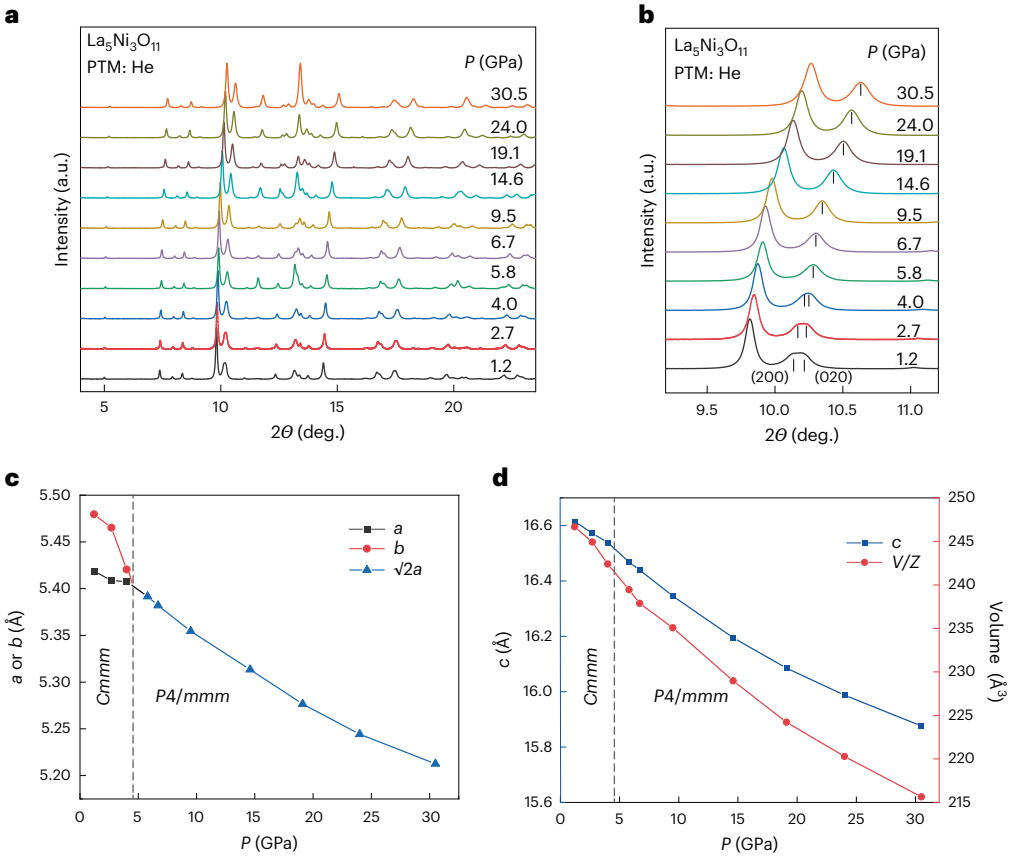

Fig. 4 | Structural evolution of the $La_5Ni_3O_{11}$ single crystal with pressure. **a**, Powder XRD patterns of $La_5Ni_3O_{11}$ under various pressures. **b**, Enlarged view of **a** at the 2Θ range of 9.2–11.2°, where the diffraction peaks of (200) and (020) gradually merged with increasing pressure. **c**, Calculated lattice parameters of the *a* and *b* axes for $La_5Ni_3O_{11}$ under various pressures. The values of *a* and *b* decrease quickly and become equal at approximately 4.5 GPa (dashed line). **d**, Calculated lattice parameters of the *c* axis and specific cell volume for one $La_5Ni_3O_{11}$ molecule (*V*/*Z*) under various pressures, where *V* is the cell volume and *Z* is the molecule number for one crystal cell. The dashed line is located at 4.5 GPa. PTM, pressure-transmitting medium.

is calculated to be as high as 69.7% and 70.0% at 10 Oe and 20 Oe, respectively. All these magnetic susceptibility results under high pressure confirm bulk superconductivity, and the onset temperature of the Meissner effect is quite consistent with the T_c^{zero} measured from the resistance curves. As shown in Fig. 3c,f, the same data in Fig. 3a,d are plotted in $4\pi\chi$ as a function of temperature.

Structural transition under pressure

To further understand the electrical transport behaviour under pressure, we measured the powder XRD patterns under various pressures up to 30.5 GPa for the hybrid 1212 nickelate by grinding several pieces of microcrystals with helium gas as the pressure-transmitting medium at the Shanghai Synchrotron Radiation Facility at a wavelength of 0.4834 Å. Figure 4 and Extended Data Fig. 5 summarize the main results. At ambient pressure, the 1212 nickelate microcrystal adopts an orthorhombic structure with a space group of *Cmmm*, which is characterized by the splitting of the (020) and (200) diffraction peaks. With increasing pressure, the diffraction peaks of (020) and (200) gradually merged, which indicates a structural transition from the orthorhombic phase to the tetragonal phase below 5.8 GPa (Fig. 4b). In the crystals of $La_3Ni_2O_7$ with the *Amam* space group and $La_4Ni_3O_{10}$, the pressure at which the structure transitions into the tetragonal phase is approximately 14 GPa, which is much greater than that of the hybrid RP 1212 nickelate[9,12]. The refinement of the powder XRD pattern at 5.8 GPa gives a tetragonal phase structure with a space group of *P*4/*mmm* (Extended Data Fig. 5b), which is similar to the case of the hybrid RP 1313 phase under high pressure[20]. The tetragonal phase structure is maintained at 30.5 GPa. More detailed evolution of the lattice parameters and cell volume are refined and shown in Fig. 4c,d, where the lattice parameters show a progressive decrease under pressure. A careful analysis of the evolution of the lattice parameters of the *a* and *b* axes indicates that the critical pressure for the structural transition is approximately 4.5 GPa (Fig. 4c).

Pressure-dependent phase diagram

In Fig. 5a, we summarize the results of high-pressure transport and XRD diffraction into a pressure-dependent phase diagram. As the pressure increases, the crystalline structure of the hybrid RP 1212 nickelate transitions from a low-pressure orthorhombic phase (*Cmmm*) to a high-pressure tetragonal phase (*P*4/*mmm*) at a critical pressure of ~4.5 GPa, which is much lower than that of $La_3Ni_2O_7$ and $La_4Ni_3O_{10}$ (~14 GPa)[9,11]. In contrast to previous high-pressure transport measurements on $La_3Ni_2O_7$ and $La_4Ni_3O_{10}$, the DW transition in 1212 nickelate is quite robust during the structural transition. In addition to a small jump at ~4.5 GPa, the DW transition temperature continuously increases with increasing pressure. The small jump in the DW transition temperature at ~4.5 GPa suggests that the structural transition slightly affects the DW transition. This might be related to the change in the Fermi surface due to the structural transition. Notably, previous muon spin rotation and nuclear magnetic resonance experiments on pressurized $La_3Ni_2O_7$ revealed a pressure-enhanced spin-density-wave (SDW) transition[14,15]. We speculate that the DW transition in the hybrid RP 1212 nickelate is also related to a similar SDW transition, which needs further experimental investigation in the future. Above 11.7 GPa, the superconducting phase emerges with dome-like pressure-dependent behaviour. Our present results indicate strong competition between

https://doi.org/10.1038/s41567-025-03023-3

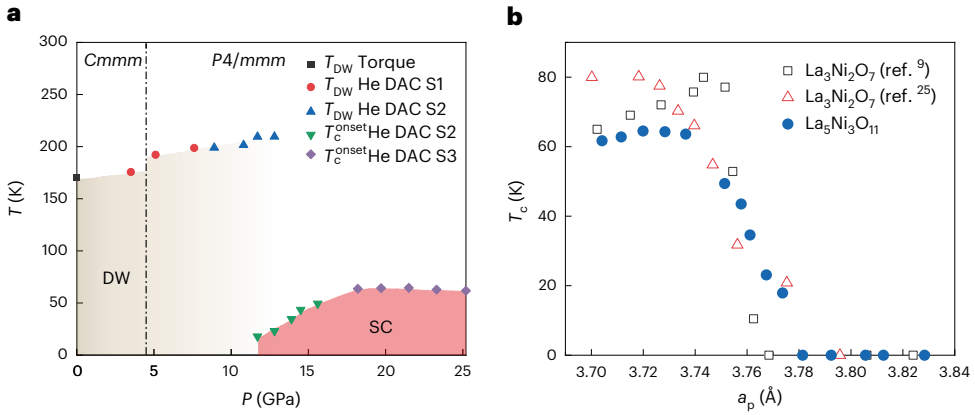

Fig. 5 | Phase diagram of the hybrid RP 1212 nickelates with the chemical formula $La_5Ni_3O_{11}$. a, Pressure-dependent crystal structure, DW transition and T_c^{onset} for the $La_5Ni_3O_{11}$ single crystal. The dotted dashed line separates the crystal structures of *Cmmm* and *P4/mmm*. The grey and red areas indicate the DW regime (DW) and superconductivity regime (SC), respectively. **b**, The T_c^{onset} and the average in-plane lattice (a_p) relationship for $La_5Ni_3O_{11}$.

possible SDW order and superconductivity. They are connected via a first-order phase transition in the pressure-dependent phase diagram. Previous studies on the pressure-dependent phase diagram in RP nickelate superconductors suggest that the tetragonal structure plays an important role in high-pressure superconductivity[11,22]. However, this picture is challenged by our recent work on both tetragonal $La_4Ni_3O_{10}$ and $La_3Ni_2O_7$ (refs. 23,24). Our results for both $La_4Ni_3O_{10}$ and $La_3Ni_2O_7$ indicate that the DW transition, rather than the tetragonal structure, plays a key role in the superconductivity under high pressure. Although superconductivity appears only when the DW transition is suppressed under high pressures, the DW transition at ambient pressure is necessary for the emergence of superconductivity under high pressure. Here, in $La_5Ni_3O_{11}$, the absence of any effect on superconductivity from the structural transition further supports the above proposed picture, in which the tetragonal structure is not a necessary ingredient for superconductivity. As shown in Extended Data Table 2, we performed a more detailed comparative analysis of the DW transition temperatures, the onset pressures for superconductivity and the optimal superconducting transition temperatures across three RP nickelate superconductors, $La_3Ni_2O_7$, $La_4Ni_3O_{10}$ and $La_5Ni_3O_{11}$. We found that the DW transition temperature and onset pressure for superconductivity are comparable in these three RP nickelates, suggesting a comparable energy scale for the DW state of RP nickelates. In contrast, the optimal superconducting transition temperature differs remarkably among different RP nickelates. Since both $La_3Ni_2O_7$ and $La_5Ni_3O_{11}$ contain the same bilayer Ni–O structure, the optimal superconducting transition temperature is comparable in these two RP phases and shows an anticorrelation with the DW transition temperature, supporting a competitive character between the DW state and superconductivity. However, both the DW transition temperature and optimal superconducting transition temperature are lower in $La_4Ni_3O_{10}$. Considering the structural difference between the bilayer Ni–O structure and the trilayer Ni–O structure, interlayer coupling might also play an important role in both the DW state and superconductivity in RP nickelates. Understanding the underlying physics is beyond the present scope, but would stimulate further theoretical investigations in the future.

Finally, we also studied the relationship between T_c and the average in-plane lattice ($a_p = \frac{1}{2}\sqrt{a^2 + b^2}$) in the hybrid RP 1212 nickelate. As shown in Fig. 5b, the relationship between the T_c and the average in-plane lattice parameter in 1212 nickelate is similar to that in pressurized $La_3Ni_2O_7$ (refs. 9,25), in which pressure-induced superconductivity appears in the structure with a relatively small a_p (<3.77 Å). This result suggests that the multilayer perovskite structure $(RNiO_3)_3$ is the fundamental building block for superconductivity. Very recently, by utilizing compressed strain through a substrate, ambient-pressure superconductivity has been observed in $La_{3-x}Pr_xNi_2O_7$ films[26,27]. The relationship between T_c and the average in-plane lattice in these $La_{3-x}Pr_xNi_2O_7$ films also shows a similar behaviour as that of the bulk samples under pressure. Here the observation of pressure-induced superconductivity in the hybrid RP 1212 nickelate suggests an alternative route to achieve ambient-pressure superconductivity in the hybrid RP nickelates. The average in-plane lattice parameter of La_2NiO_4 is approximately 3.85–3.87 Å, which is relatively larger than the average in-plane lattice parameter of $La_3Ni_2O_7$ (a_p = 3.835 Å)[28]. If we can replace the La_2NiO_4 layer with another RP layer with a smaller a_p, it might be possible to tune the value of a_p to the superconducting region, as shown in Fig. 5b. This deserves further experimental exploration of new hybrid RP nickelates.

In summary, bulk superconductivity with an optimal T_c^{onset} of approximately 64 K was achieved in hybrid RP 1212 nickelate ($La_5Ni_3O_{11}$) single crystals, which extends the superconducting member in the RP nickelate family. The pressure-dependent phase diagram of $La_5Ni_3O_{11}$ further reveals a first-order phase transition between the low-pressure DW order and the high-pressure superconductivity. In addition, a structural transition from the orthorhombic phase to the tetragonal phase is also observed at lower pressures before the emergence of superconductivity. All these results strongly suggest an underlying interplay between DW order and superconductivity in $La_5Ni_3O_{11}$. More theoretical and experimental investigations at microscopic scale are urgently needed to study the correlation between DW order on superconductivity in $La_5Ni_3O_{11}$, which would shed new light on the superconducting mechanism.

Online content

Any methods, additional references, Nature Portfolio reporting summaries, source data, extended data, supplementary information, acknowledgements, peer review information; details of author contributions and competing interests; and statements of data and code availability are available at https://doi.org/10.1038/s41567-025-03023-3.

References

1. Bednorz, J. G. & Müller, K. A. Possible high T_c superconductivity in the Ba–La–Cu–O system. *Z. Phys. B: Condens. Matter* **64**, 189–193 (1986).
2. Norman, M. R. Materials design for new superconductors. *Rep. Prog. Phys.* **79**, 074502 (2016).
3. Azuma, M., Hiroi, Z., Takano, M., Bando, Y. & Takeda, Y. Superconductivity at 110 K in the infinite-layer compound $(Sr_{1-x}Ca_x)_{1-y}CuO_2$. *Nature* **356**, 775–776 (1992).
4. Anisimov, V. I., Bukhvalov, D. & Rice, T. M. Electronic structure of possible nickelate analogs to the cuprates. *Phys. Rev. B* **59**, 7901–7906 (1999).

5. Lee, K.-W. & Pickett, W. E. Infinite-layer $LaNiO_2$: Ni^{1+} is not Cu^{2+}. *Phys. Rev. B* **70**, 165109 (2004).
6. Crespin, M., Levitz, P. & Gatineau, L. Reduced forms of $LaNiO_3$ perovskite. Part 1.—Evidence for new phases: $La_2Ni_2O_5$ and $LaNiO_2$. *J. Chem. Soc. Faraday Trans.* **79**, 1181–1194 (1983).
7. Hayward, M. A., Green, M. A., Rosseinsky, M. J. & Sloan, J. Sodium hydride as a powerful reducing agent for yopotactic oxide deintercalation: synthesis and characterization of the nickel(I) oxide $LaNiO_2$. *J. Am. Chem. Soc.* **121**, 8843–8854 (1999).
8. Li, D. et al. Superconductivity in an infinite-layer nickelate. *Nature* **572**, 624–627 (2019).
9. Sun, H. et al. Signatures of superconductivity near 80 K in a nickelate under high pressure. *Nature* **621**, 493–498 (2023).
10. Li, Q. et al. Signature of superconductivity in pressurized $La_4Ni_3O_{10}$. *Chin. Phys. Lett.* **41**, 017401 (2024).
11. Zhu, Y. et al. Superconductivity in tri-layer nickelate $La_4Ni_3O_{10}$ single crystals. *Nature* **631**, 531–536 (2024).
12. Zhang, M. et al. Superconductivity in tri-layer nickelate $La_4Ni_3O_{10}$ under pressure. *Phys. Rev. X* **15**, 021005 (2025).
13. Sakakibara, H. et al. Theoretical analysis on the possibility of superconductivity in the tri-layer Ruddlesden–Popper nickelate $La_4Ni_3O_{10}$ under pressure and its experimental examination: comparison with $La_3Ni_2O_7$. *Phys. Rev. B* **109**, 144511 (2024).
14. Dan, Z. et al. Pressure-enhanced spin-density-wave transition in double-layer nickelate $La_3Ni_2O_{7-\delta}$. *Sci. Bull.* **70**, 1239–1245 (2025).
15. Chen, K. et al. Evidence of spin density waves in $La_3Ni_2O_{7-\delta}$. *Phys. Rev. Lett.* **132**, 256503 (2024).
16. Zhang, J. et al. Intertwined density waves in a metallic nickelate. *Nat. Commun.* **11**, 6003 (2020).
17. Zhang, Y. et al. High-temperature superconductivity with zero resistance and strange-metal behavior in $La_3Ni_2O_{7-\delta}$. *Nat. Phys.* **20**, 1269–1273 (2024).
18. Li, F. et al. Design and synthesis of three-dimensional hybrid Ruddlesden–Popper nickelate single crystals. *Phys. Rev. Mater.* **8**, 053401 (2024).
19. Chen, X. et al. Polymorphism in the Ruddlesden–Popper nickelate $La_3Ni_2O_7$: discovery of a hidden phase with distinctive layer stacking. *J. Am. Chem. Soc.* **146**, 3640–3645 (2024).
20. Puphal, P. et al. Unconventional crystal structure of the high-pressure superconductor $La_3Ni_2O_7$. *Phys. Rev. Lett.* **133**, 146002 (2024).
21. Shulga, S. V. et al. Upper critical field peculiarities of superconducting YNi_2B_2C and $LuNi_2B_2C$. *Phys. Rev. Lett.* **80**, 1730 (1998).
22. Wang, N. et al. Bulk high-temperature superconductivity in pressurized tetragonal $La_2PrNi_2O_7$. *Nature* **634**, 579–584 (2024).
23. Shi, M. et al. Absence of superconductivity and density-wave transition in ambient-pressure tetragonal $La_4Ni_3O_{10}$. *Nat. Commun.* **16**, 2887 (2025).
24. Shi, M. et al. Prerequisite of superconductivity: SDW rather than tetragonal structure in double-layer $La_3Ni_2O_{7-x}$. Preprint at https://arxiv.org/abs/2501.14202 (2025).
25. Li, J. et al. Identification of the superconductivity in bilayer nickelate $La_3Ni_2O_7$ upon 100 GPa. *Natl Sci. Rev.* **12**, nwaf220 (2025).
26. Liu, Y. et al. Superconductivity and normal-state transport in compressively strained $La_2PrNi_2O_7$ thin films. *Nat. Mater.* **24**, 1221–1227 (2025).
27. Zhou, G. et al. Ambient-pressure superconductivity onset above 40 K in $(La,Pr)_3Ni_2O_7$ films. *Nature* **640**, 641–646 (2025).
28. Thanh, T. D. et al. Structure, magnetic, and electrical properties of $La_2NiO_{4+\delta}$ compounds. *IEEE Trans. Magn.* **53**, 8204904 (2017).
29. Prozorov, R. & Kogan, V. G. Effective demagnetizing factors of diamagnetic samples of various shapes. *Phys. Rev. App.* **10**, 014030 (2018).
30. Wang, G. et al. Pressure-induced superconductivity in poly-crystalline $La_3Ni_2O_{7-\delta}$. *Phys. Rev. X* **14**, 011040 (2024).

Publisher's note Springer Nature remains neutral with regard to jurisdictional claims in published maps and institutional affiliations.

Springer Nature or its licensor (e.g. a society or other partner) holds exclusive rights to this article under a publishing agreement with the author(s) or other rightsholder(s); author self-archiving of the accepted manuscript version of this article is solely governed by the terms of such publishing agreement and applicable law.

© The Author(s), under exclusive licence to Springer Nature Limited 2025

[1]Hefei National Research Center for Physical Sciences at the Microscale, University of Science and Technology of China, Hefei, China. [2]Department of Physics, University of Science and Technology of China, Hefei, China. [3]Shanghai Key Laboratory of Material Frontiers Research in Extreme Environments (MFree), Institute for Shanghai Advanced Research in Physical Sciences (SHARPS), Shanghai, China. [4]Center for High Pressure Science and Technology Advanced Research, Shanghai, China. [5]Information Materials and Intelligent Sensing Laboratory of Anhui Province, Anhui Key Laboratory of Magnetic Functional Materials and Devices, Institutes of Physical Science and Information Technology, Anhui University, Hefei, China. [6]Shanghai Synchrotron Radiation Facility, Shanghai Advanced Research Institute, Chinese Academy of Sciences, Shanghai, China. [7]Hefei National Laboratory, University of Science and Technology of China, Hefei, China. [8]Collaborative Innovation Center of Advanced Microstructures, Nanjing University, Nanjing, China. [9]These authors contributed equally: Mengzhu Shi, Di Peng. ✉e-mail: zengqs@hpstar.ac.cn; wutao@ustc.edu.cn; chenxh@ustc.edu.cn

Methods

Sample growth

The $La_5Ni_3O_{11}$ crystals were grown via a molten-salt method. First, the $La_5Ni_3O_x$ precursor (P) was obtained via a standard sol-gel process. Specifically, the La source (lanthanum nitrate hexahydrate), Ni source (nickel (II) nitrate hexahydrate) and complexing agent (citric acid (CA)) were dissolved in water at a molar ratio of La:Ni:CA = 5:3:8. The above solution was preheated at 140 °C for approximately 24 h to obtain a dry gel, which was then transferred into a muffle furnace where the temperature was slowly increased to 400 °C and maintained for another 10 h. Second, the above precursor (P) was mixed with a salt flux (NaCl/KCl mixture) at a mass ratio of P:NaCl:KCl = 1:14:16 and loaded into a corundum crucible. The corundum crucible was heated to 1150 °C for 10 h, maintained at this temperature for 48 h, and then slowly cooled to 1110 °C within 7 days. Microcrystals with a typical size of 0.1 × 0.1 × 0.02 mm were obtained after the flux was washed with water.

Structural and composition characterization at ambient pressure

The as-grown microcrystal was mounted on the sample holder using high-vacuum silicon grease as the glue. SC-XRD data were collected on a four-circle diffractometer (Rigaku, XtaLAB PRO 007HF) with Cu Kα radiation at the Core Facility Center for Life Sciences in the University of Science and Technology of China. The structure was solved and refined via Olex-2 with the ShelXT and ShelXL packages. The detailed structural data are shown in Extended Data Table 1. All the crystals were first checked via a four-circle diffractometer before they were used to conduct further physical measurements. EDX equipped with a scanning electron microscope (Hitachi SU8220) was used to characterize the chemical composition. The element ratio of La:Ni is approximately 1.67:1 (Extended Data Fig. 2). The refinement of the occupancy of the oxygen sites on the basis of the SC-XRD data gives a value of 0.984–1.072, which indicates nearly full occupation of all these oxygen sites. There is only one oxygen site (O3 site; Fig. 1a) that is smaller than 1. These results indicate negligible non-stoichiometry in the as-grown $La_5Ni_3O_{11}$ single crystal. The STEM images were collected on a Thermo Fisher Scientific Titan Themis Z microscope with a working voltage of 300 kV.

Magnetic torque measurement

Using an SCL piezo-resistive cantilever, torque magnetometry data were collected via a physical property measurement system (PPMS, Quantum Design Inc., DynaCool-14T). The sample was carefully attached to the tip of the cantilever, which was fixed on a horizontal rotator. The sample was rotated in the range of θ (the angle between the magnetic field vector H (14 T) and the flat plane of the $La_5Ni_3O_{11}$ crystal) from 0° to 90° under isothermal conditions.

Electrical transport and XRD measurements and magnetic susceptibility under high pressure

Resistance curves for the $La_5Ni_3O_{11}$ single crystals under high pressure were measured in a DAC using helium gas as the pressure-transmitting medium. The pressure was applied, and the mixture was calibrated by shifting the ruby florescence at room temperature. The transport measurements were conducted in a physical properties measurement system (PPMS-9, Quantum Design Inc.). The powder XRD data of $La_5Ni_3O_{11}$ under pressure were collected by gridding several pieces of microcrystals at the Shanghai Synchrotron Radiation Facility via an X-ray beam with a wavelength of 0.4834 Å. Helium gas was used as the pressure-transmitting medium. The powder XRD data were refined via GSAS software to obtain the lattice parameters under different pressures.

Direct-current magnetic susceptibility measurements under pressure were conducted via a custom-built miniature DAC. The beryllium–copper alloy DAC was integrated with a magnetic property measurement system (MPMS3, Quantum Design Inc.). The cell design featured paired diamond anvils 400 μm in diameter. Non-magnetic rhenium gaskets were employed to reduce magnetic background interference. A cylindrical sample chamber 310 μm in diameter was created within the gasket. Specifically, we loaded a $La_5Ni_3O_{11}$ single crystal with planar dimensions of ~210 μm in diameter and 20 μm in thickness. Helium gas served as the pressure-transmitting medium to maintain optimal hydrostatic conditions throughout the pressure experiments. The demagnetization factor (N) for the cylindrical sample under an axial magnetic field was estimated to be $N^{-1} = 1 + 1.6 \times (C/A)$, where A is the diameter and C is the thickness of the sample[29,30]. The N is calculated as 0.8678. The superconducting volume fraction (SF) is corrected via the formula $SF = \chi/(1 - N \times \chi)$, where χ is the magnetic susceptibility without considering the demagnetization factor. The estimated superconducting volume fraction for $La_5Ni_3O_{11}$ at 22.8 GPa is approximately 74.5% and 72.8% at 10 Oe and 20 Oe, respectively.

Error-bar analysis for calculating the superconducting volume fraction

The primary sources of error in calculating the superconducting volume fraction stem from three main factors: the background signal, the residual magnetic field within the measurement system and the estimation of the sample's diameter and thickness. The temperature at which the strongest diamagnetic signal occurs is denoted as T_c^{most}. The background signal at temperatures below T_c^{onset} is estimated through a linear extrapolation of the magnetic susceptibility data from the normal state. The error bar for the background signal is estimated to be half the difference in the background signal between T_c^{onset} and T_c^{most}. The error in the residual magnetic field within the measurement system is estimated to be less than or equal to 0.2 Oe. The sample's diameter and thickness were measured using microscopy. The sample is considered to be a circular plate with an average diameter of 210 μm and a thickness of 20 μm. The diameter error (±5 μm) arises from the irregular shape, while the thickness error (±1 μm) originates from the resolution of the microscope. After analysing these errors, the error bar for the superconducting volume fraction is calculated to be between 2% and 3%. More detailed values for the error bar are presented in the caption of Fig. 3.

Data availability

The data supporting the findings of this study are available via figshare at https://doi.org/10.6084/m9.figshare.29484635 (ref. 31). The detailed crystal structure data from this study have been deposited in the Cambridge Crystallographic Data Centre (CCDC) website with the deposition number CSD 2469506. These data are available from the corresponding author upon request. Source data are provided with the paper.

Code availability

The codes that support the findings of this study are available from the corresponding author upon request.

References

31. Shi, M. et al. Pressure induced superconductivity in hybrid Ruddlesden–Popper $La_5Ni_3O_{11}$ single crystals. Raw Data. *figshare* https://doi.org/10.6084/m9.figshare.29484635 (2025).

Acknowledgements

We acknowledge fruitful discussions with H. Mao, Z. Wang and Z. Xiang. We also thank Z. Zhu, F. Lan, Y. Liu and H. Lou for their experimental assistance. This work is supported by the National Key R&D Programme of the MOST of China (Grant No. 2022YFA1602601 (to X.C. and T.W.)), the National Natural Science Foundation of China (Grant Nos 12494592 (to M.S. and J.Y.), 12488201 (to X.C.), 11888101

(to X.C.), 12034004 (to T.W.), 12161160316 (to T.W.), 12325403 (to T.W.) and 12204448 (to M.S.)), the Chinese Academy of Sciences under contract no. JZHKYPT-2021-08 (to X.C., T.W. and J.Y.), the CAS Project for Young Scientists in Basic Research (Grant No. YBR-048 (to J.Y., T.W. and M.S.)) and the Innovation Programme for Quantum Science and Technology (Grant No. 2021ZD0302800 (to T.W. and X.C.)). D.P. and Q.Z. acknowledge the financial support from the Shanghai Science and Technology Committee (Grant No. 22JC1410300 (to Q.Z. and D.P.)) and Shanghai Key Laboratory of Material Frontiers Research in Extreme Environments (Grant No. 22dz2260800 (to Q.Z. and D.P.)). A portion of this research used resources at the beamline 17UM of the Shanghai synchrotron radiation facility (https://cstr.cn/31124.02.SSRF.BL17UM).

Author contributions

X.C. conceived the research project and coordinated the experiments. M.S. grew the single crystals and performed the structural characterization at ambient pressure with the help of R.W. and M.D. H.L. and K.F. measured the magnetic torque data. S.Y. and B.G. collected the TEM images. D.P. performed the resistance measurements using helium gas as the pressure-transmitting medium under pressure with the help of Q.Z. D.P., Z.X. and Y.W. performed the synchrotron powder diffraction measurements and analysis under high pressure using helium gas as the pressure-transmitting medium with help from Q.Z. and Z.Z. M.S., D.P., J.Y., T.W. and X.C. analysed the data. M.S., D.P., K.F., T.W. and X.C. wrote the paper with input from all the authors.

Competing interests

The authors declare no competing interests.

Additional information

Extended data is available for this paper at https://doi.org/10.1038/s41567-025-03023-3.

Supplementary information The online version contains supplementary material available at https://doi.org/10.1038/s41567-025-03023-3.

Correspondence and requests for materials should be addressed to Qiaoshi Zeng, Tao Wu or Xianhui Chen.

Peer review information *Nature Physics* thanks Weiwei Xie and the other, anonymous, reviewer(s) for their contribution to the peer review of this work.

Reprints and permissions information is available at www.nature.com/reprints.

https://doi.org/10.1038/s41567-025-03023-3

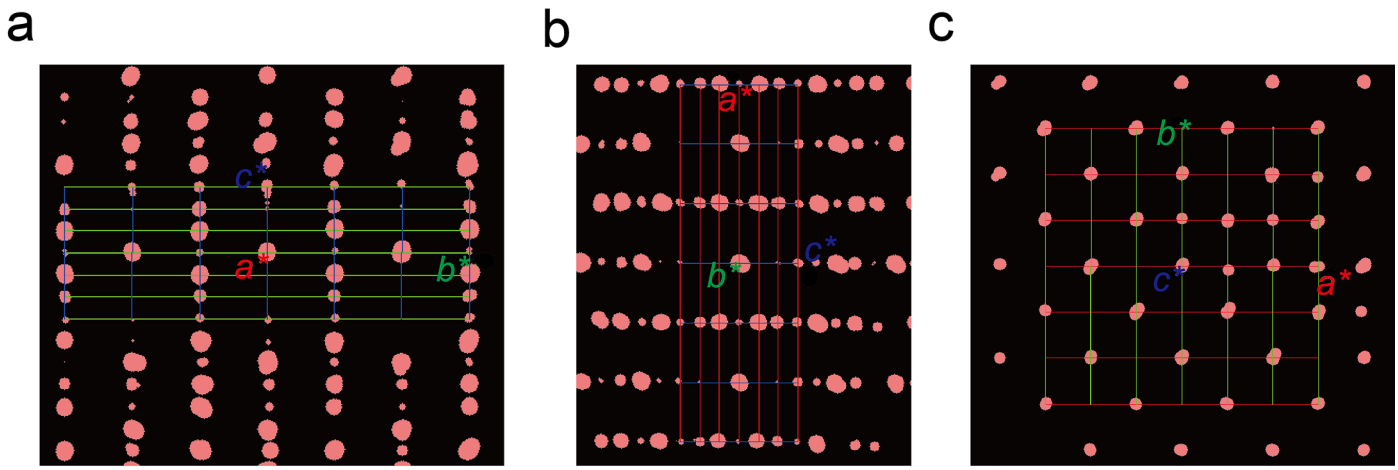

Extended Data Fig. 1 | Reciprocal lattice data. (**a**)–(**c**), Reciprocal lattice data of $La_5Ni_3O_{11}$ along the a^*, b^* and c^* axes, respectively. The size of the spots represents the intensity of the diffraction peaks.

https://doi.org/10.1038/s41567-025-03023-3

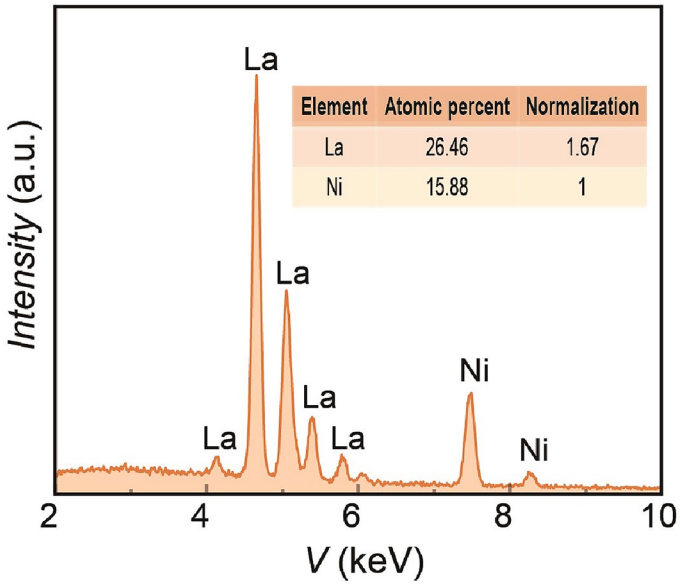

Element	Atomic percent	Normalization
La	26.46	1.67
Ni	15.88	1

Extended Data Fig. 2 | EDX results of the as-grown microcrystals. The element ratio is La:Ni = 1.67:1, which is consistent with the chemical formula of $La_5Ni_3O_{11}$.

https://doi.org/10.1038/s41567-025-03023-3

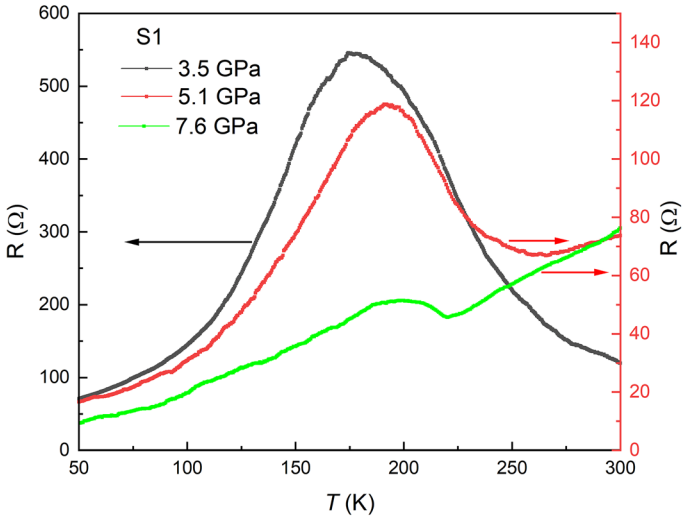

Extended Data Fig. 3 | Resistance curves for sample S1. Temperature-dependent resistance curves for $La_5Ni_3O_{11}$ (S1) at various pressures.

https://doi.org/10.1038/s41567-025-03023-3

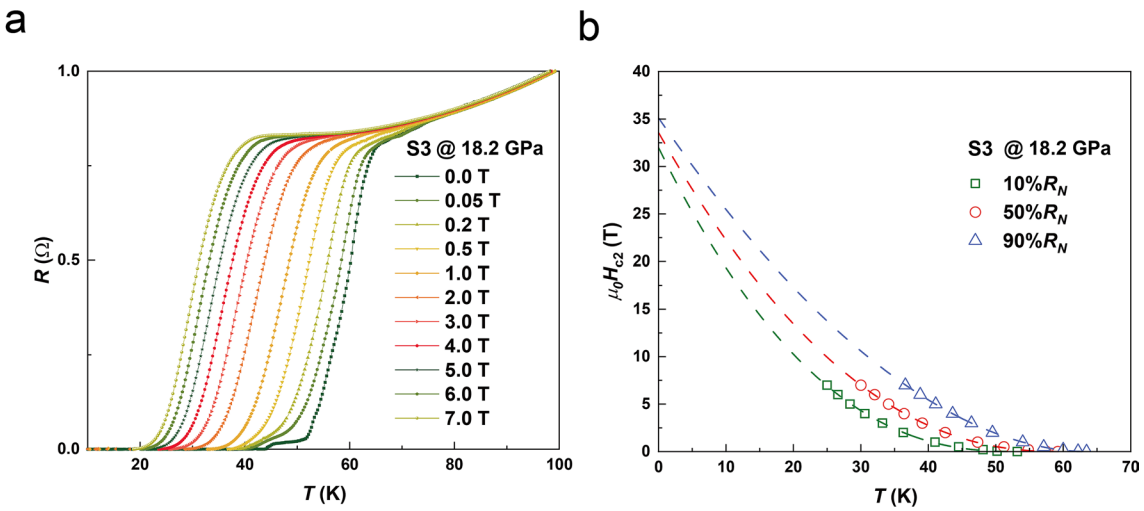

Extended Data Fig. 4 | Superconductivity and the upper critical field. (**a**) $R(T)$ curves for $La_5Ni_3O_{11}$ (S3) at 18.2 GPa under various magnetic fields along the *c*-axis direction. The onset T_c is quickly suppressed to a lower temperature with increasing magnetic field. (**b**) The upper critical field extracted with different criteria in (**a**), where the R_N is the resistance at the normal state. There is an obvious positive curvature in the H_{c2}-T_c curve. The upper critical field at the zero-temperature limit is fitted via the two-band model at the clean limit.

https://doi.org/10.1038/s41567-025-03023-3

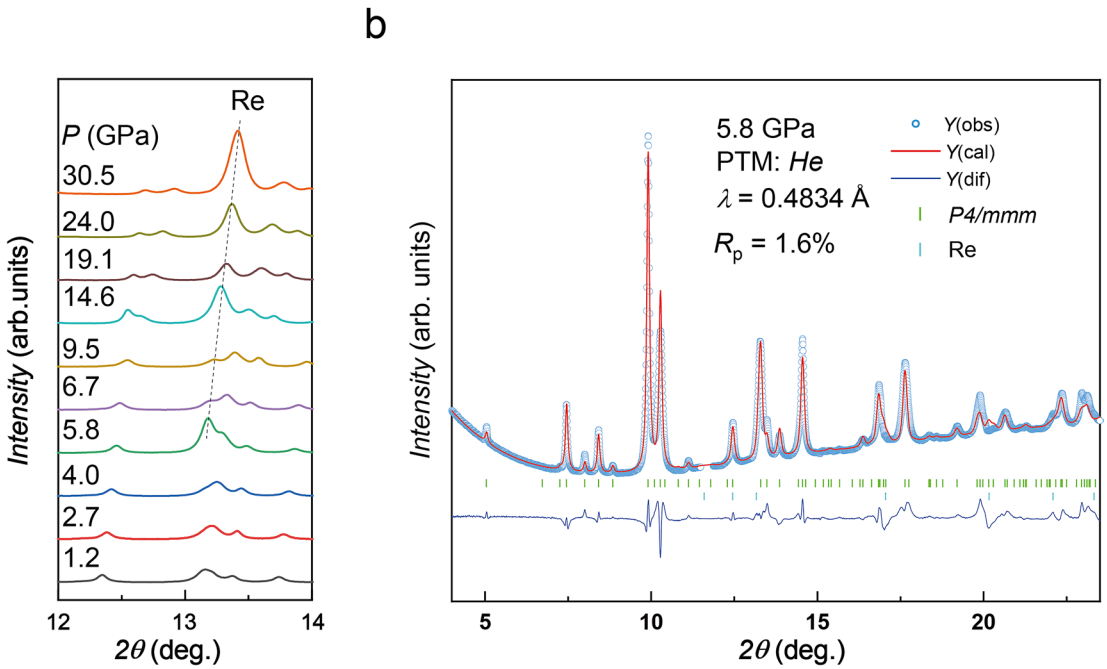

Extended Data Fig. 5 | Powder XRD patterns of the $La_5Ni_3O_{11}$ crystal under various pressures. (**a**) Powder XRD patterns of the $La_5Ni_3O_{11}$ crystal under various pressures in the 2θ range of 12–14°, where the dashed line indicates the signal from the gasket (Re). (**b**) Rietveld refinement of the powder XRD pattern for $La_5Ni_3O_{11}$ at 5.8 GPa. The collected data can be well fitted via the space group *P4/mmm*. The blue circles and red lines represent the observed and calculated data, respectively. The blue lines indicate the difference between the observed and calculated data. The short green and cyan vertical lines indicate the calculated diffraction peak positions of $La_5Ni_3O_{11}$ with *P4/mmm* space group and Re.

https://doi.org/10.1038/s41567-025-03023-3

Extended Data Table 1 | Crystal data, structure refinement and bond angle for $La_5Ni_3O_{11}$

Identification code	LNO1212
Empirical formula	$La_5Ni_3O_{11}$
Formula weight	1046.68
Temperature/K	300.4(4)
Crystal system	orthorhombic
Space group	*Cmmm*
a/Å	5.4264(5)
b/Å	5.4485(5)
c/Å	16.5750(12)
α/°	90
β/°	90
γ/°	90
Volume/Å^3	490.05(7)
Z	2
ρ_{calc} g/cm^3	7.093
μ/mm^{-1}	171.053
F(000)	914
Crystal size/mm^3	0.073 × 0.052 × 0.007
Radiation	Cu *Kα* (λ = 1.54184 Å)
2*Θ* range for data collection/°	10.674 to 156.012
Index ranges	$-6 \le h \le 6$, $-6 \le k \le 6$, $-21 \le l \le 20$
Reflections collected	2823
Independent reflections	330 [R_{int} = 0.0610, R_{sigma} = 0.0303]
Data/restraints/parameters	330/0/39
Goodness-of-fit on F^2	1.112
Final *R* indexes [I>=2*σ* (I)]	R_1 = 0.0453, wR_2 = 0.1244
Final *R* indexes [all data]	R_1 = 0.0463, wR_2 = 0.1253
Largest diff. peak/hole / e Å^{-3}	3.97/-3.00
In-plane Ni-O/Å	Ni1-O2: 1.922 Ni2-O4: 1.922
Out-of-plane Ni-O/Å	Ni1-O1: 2.217 Ni2-O3: 2.236 Ni2-O5: 1.985
In-plane Ni-O-Ni/deg.	Ni1-O2-Ni1: 180 Ni2-O4-Ni2: 180
Out-of-plane Ni-O-Ni/deg.	Ni2-O5-Ni2: 180

https://doi.org/10.1038/s41567-025-03023-3

Extended Data Table 2 | Comparison of density-wave transition temperatures, optimal superconducting transition temperatures and onset pressures for superconductivity in $La_3Ni_2O_7$, $La_4Ni_3O_{10}$ and $La_5Ni_3O_{11}$

Compound	T_{DW} (K)	T_c onset (K)	P_c (GPa)
$La_3Ni_2O_7$	130-150 (9,17,30)	80 (9,30)	13 (17)
$La_4Ni_3O_{10}$	136 (11)	30 (11)	15.5 (11)
$La_5Ni_3O_{11}$	170	64	11.7